IEEE Access
Multidisciplinary | Rapid Review | Open Access Journal

Received November 17, 2019, accepted December 4, 2019, date of publication December 9, 2019,
date of current version December 23, 2019.

Digital Object Identifier 10.1109/ACCESS.2019.2958387

Signal Measurement of Projectile Penetration Overload Based on Charge Sensor

DEBIAO ZHANG[1], JIE LI[1,2], XIAOKAI WEI[1], KAIQIANG FENG[1], YU WANG[1], AND JIHE ZHAO[1]

[1]Key Laboratory of Instrumentation Science and Dynamic Measurement, North University of China, Taiyuan 030051, China
[2]National Key Laboratory for Electronic Measurement Technology, North University of China, Taiyuan 030051, China

Corresponding author: Jie Li (lijie@nuc.edu.cn)

This work was supported in part by the National Natural Science Funds for Distinguished Young Scholars under Grant 51225504, in part by the National Natural Science Foundation of China under Grant 51575500 and Grant 51705477, and in part by the Foundation for Middle-Aged and Young Talents in Higher Education Institutions.

ABSTRACT In modern warfare, in order to destroy the target to largest extent, missile warhead is required to explode after penetrating inside the target, therefore, the measurement of mechanical signal during projectile penetration is critical. This paper studies the dynamic design principle of projectile penetration overload test system based on charge sensor, according to characteristics of steep front and a great number of contained installing structure impulse response, designs the measuring circuit based on charge sensor, conducts detailed theoretical deduction on dynamic model of sensor, charge-amplifier, filter and single conversion differential circuit, and provides theoretical basis for design. In order to more objectively evaluate the dynamic characteristics of this kind of test system, the dynamic uncertainty estimation of charge signal measured by this test system is considered as the standard for evaluating its dynamic characteristics, instead of unflatness of amplitude-frequency characteristic and its width in frequency domain, and the comprehensive evaluation on uncertainty of this test system is realized. In order to improve the measurement accuracy of dynamic test system designed, in this paper, an improved de-noising algorithm based on Ensemble Empirical Mode Decomposition (EEMD) is proposed, different low-pass filters are formed on the basis of Intrinsic Mode Function (IMF), de-noising effect of signal with noise is analyzed, and the evaluation indicators of dynamic uncertainty and approximation are established. Finally, the effectiveness of the designed method is verified through experiment.

INDEX TERMS Charge sensor, penetration overload, dynamic design, dynamic uncertainty, EEMD.

I. INTRODUCTION

In modern warfare, in order to destroy the target to largest extent, missile warhead is required to explode after penetrating inside the target, relying on impulse wave caused by loaded explosion inside warhead to destroy target, therefore, the measurement of mechanical signal in projectile penetration is critical. The projectile can travel through different media in penetration, with the impact of carrier structure, impulse acceleration signal include the steep front and a large number of impulse response of installing structure, thus, it is necessary to design measuring circuit according to characteristics of impulse penetration signal, so as to improve measurement accuracy.

The associate editor coordinating the review of this manuscript and approving it for publication was Chengpeng Hao.

D.J. Frew, M.J. Forrestal et al perform a large quantity of researches on the penetration of concrete and geological targets, and establish mathematical model of penetration, which provide such information as penetration depth, impact velocity and penetration model. And the experimentally established mathematical model was verified by experiments [1]–[5]. Warren present a method to correct the deceleration data so that an integration of the deceleration data agreed with the measured striking velocity. These corrections were small, and a double integration of the corrected deceleration was in good agreement with the measured depth of penetration [6]. In [7], An explicit dimensionless expression for predicting the terminal ballistic parameters of the projectile perforating the RC slab was proposed and well validated. In [8], Several perforation tests using concrete targets of different thicknesses were conducted with a nominal

striking velocity of 400 m/s. The residual velocity and kinetic energy consumed versus the target thickness was analyzed. The perforation limit was also obtained. Z.C.Lu propose a theoretical model for the penetration of semi-infinite metal targets struck transversely by high strength long rod penetrators within a unified framework with emphasis being placed upon non-rigid penetration. In particular, the hydrodynamic velocity (VH) will be re-defined on basis of physical concept. Secondary penetration will also be considered [9]. In the present study of Liu Jian, impact responses of UHPC targets with 3 vol-% ultra-high molecular weight polyethylene (UHMWPE) fibres and UHPC targets with 3 vol-% steel fibres are experimentally investigated subjected to high-velocity projectile penetration, and plain concrete targets under the same loading scenarios are also tested as control specimens for comparative purpose [10]. A series of scaled penetration experiments with ogive-nosed, steel projectiles penetrating into medium strength concrete cylindrical targets were conducted in Chen Xuguang's paper. In these experiments, the projectiles are launched with the velocity of 800 to 900 m/s at a certain angle. The three-dimensional flight attitudes of the projectile are recorded with a designed high-speed camera system [11]. Liu Jian numerically investigates the effects of steel wire mesh reinforcement on reactive powder concrete (RPC) targets subjected to high-velocity projectile penetration. A numerical model based on a computer program called LS-DYNA was validated with experimental data concerning the depth of penetration (DOP) and crater diameter of reinforced RPC targets [12].

The above scholars have conducted in-depth study on penetration, established penetration model of penetrating different targets and performed many experiments. The studies show that impulse acceleration signal include steep front and a large number of impulse response of installing structure. The accurate measurement of penetration signal is required to consider characteristics of penetration signal and resonant frequency and working band of sensor, which is the necessary basis for designing measuring circuit.

Addabbo Tommaso propose a smart measurement system with improved low-frequency response to detect moving charged debris, to be used for turbomachinery condition monitoring. The postprocessing is based on the theoretical analysis of the physical experiment, assuming to use a first-order high-pass charge amplifier, with the introduction of a fitting model based on the linear combination of Gaussian functions [13]. The time-domain analysis is conducted on measurement system in detail in this paper for designing the system. A new control system for automated drift compensation of the charge amplifier periodic output voltage has been developed by Kos Tomaz. The proposed solution consists of a PI controller, which attempts to minimize drift by adjusting its output voltage, and a supervisory controller, which calculates PI controller parameters and sets the sampling frequency of the data acquisition card [14]. Kos Tomaz mainly solves the deviation of output voltage of charge amplifier by virtue of controlling knowledge. The charge measurement contains an error due to the uncertainty of the first sampled point of a signal waveform. Zhang Jiajin employ a time-to-digital converter to measure the uncertainty precisely, and they design dual-LUTs method and sectional LUT correction method to improve the resolution of the charge measurement [15]. Havunen Jussi have applied a charge-sensitive preamplifier for the low-level calibration of PD calibrators. This calibration method both improves the signal-to-noise ratio and performs the analog integration of the PD pulse. The drooping response of the preamplifier is corrected using software [16]. The improvement of measurement accuracy in low charge is mainly solved. The design and performance of a new front-end acquisition system is presented in.The system is hybrid and capable of counting active channels and performing a charge measurement. It was developed to be used with muon array with resistive plate chamber (RPCs) for tagging air showers (MARTA's) RPC detectors that measure the muonic component of cosmic ray air showers [17]. The paper focuses on the design of measurement design, not detailed introduction to the design of charge amplifier. Mahbub Ifana's study is focused on the design of a fully integrated charge amplifier for respiration monitoring based on a pyroelectric sensor. Continuous efforts on improving the performances of respiration-monitoring devices have resulted in the reduction of noise and motion artefacts by increasing complexity (e.g. complex algorithms or high precision filtering) at the expense of increased power consumption [18]. Kar Sougata Kumar have presented a simple but effective capacitive sensor interfacing circuit which provides differential analog output along with modulated digital output by a sigma–delta modulator. The analog front-end interfacing utilizes a fully differential OTA which requires single differential capacitance sensor and one feedback circuit to provide differential output [19]. However, specific indicators to assess circuit performance are not provided by the author. Marco-Hernandez Ricardo developed a Low-Noise Charge Amplifier for the ELENA Trajectory, Orbit, and Intensity Measurement System. Special attention has been paid to the amplifier printed circuit board design to minimize the parasitic capacitances and inductances at the charge amplifier stages to meet the gain and noise requirements [20]. In [21], to improve the performance of smart aggregate-based monitoring systems, a charge amplifier was designed especially for the demands of seismic stress monitoring. The designed charge amplifier mainly focuses on its low-frequency performance to monitor seismic stress, instead of middle and high-frequency performance. Seljak developed a fast, low power and low noise charge sensitive amplifier ASIC for a UV imaging single photon detector [22]. Seljak mainly studies the integration process and method, rather than the principle of charge amplifier.

The above scholars conduct various studies on the application fields of charge amplifier, with the focus on design methods in accordance with different application fields, instead of the in-depth analysis on its dynamic characteristics and evaluation methods. The main application field of this paper

is the measurement of projectile overload signal, and characteristics of steep front and a great number of contained installing structure impulse response. Therefore, this paper mainly emphasizes the dynamic characteristics of signal measurement, as well as signal processing methods in order to eliminate the influence of installing structure.

Empirical Mode Decomposition (EMD), a new signal time domain decomposition method proposed by Huang et al, especially suitable for the analysis of non-linear and non-stationary time series, is widely applied to non-linear data analysis, spectral signal and mechanical vibration signal analysis [23], [24]. Ensemble Empirical Mode Decomposition (EEMD), the improved algorithm of EMD, can effectively solve the mixing frequency [25]. According to the characteristics of steep front and a great number of contained installing structure impulse response in projectile penetration overload signal, there are multiple frequency components contained in the signal acquired, which are non stationary. Thus, the data acquired shall be effectively analyzed and processed.

This paper, according to characteristics of projectile penetration signal, designs the measuring circuit based on charge sensor, conducts detailed theoretical deduction on dynamic model of sensor, charge-amplifier, filter and single conversion differential circuit, and provides theoretical basis for design. In order to more objectively evaluate the dynamic characteristics of this kind of test system, the dynamic uncertainty estimation of charge signal measured by this test system is considered as the standard for evaluating its dynamic characteristics. According to the characteristics of steep front and a great number of contained installing structure impulse response in projectile penetration overload signal, in this paper, an improved de-noising algorithm based on EEMD is proposed, and different low-pass filters are formed on the basis of IMF. Impact factors shall be selected to determine the improved de-nosing algorithm. The validity of the designed method is verified through experiment.

II. DYNAMIC CHARACTERISTICS DESIGN OF TEST SYSTEM

The dynamic characteristics design of test system, in general, is performed in frequency domain, and the purpose is to ensure that the system can meet the requirement of dynamic characteristics by measured signal, which relates to the success or failure of test. Besides, the dynamic uncertainty estimation shall be provided because test system will record changes of measured signal within the range of tolerant dynamic uncertainty.

The sufficient and unnecessary condition of Fourier transform in measured signal is that it can satisfy Dirichlet condition. In the interval of $(-\infty, \infty)$, there are only limited discontinous points and limit points for signal, where limited value is taken.

The frequency response characteristic of test system is

$$SYS(f) = A_{senser}(f) \cdot A_{amplifier}(f) \cdot A_{filter}(f) \tag{1}$$

TABLE 1. Characteristics of sensor.

Type	Units	Range
Acceleration Range	g	±50000
Sensitivity	pC/g	-0.5
Resonant Frequency mounted	kHz	65
Frequency Response	Hz	1-12000

wherein, $SYS(f)$ is frequency response characteristic of system, $A_{senser}(f)$ is frequency response characteristic of sensor, $A_{amplifier}(f)$ is frequency response characteristic of amplifier circuit, and $A_{filter}(f)$ is frequency response characteristic of filter.

The transform between time domain and frequency domain can be completed through Fast Fourier Transform (FFT) and Inverse Fast Fourier Transform (IFFT). The specific relationship is shown in:

Measured signal $x(t)$:

$$x(t) \xrightarrow{FFT} X(f) \tag{2}$$

The relationship between frequency response characteristic and frequency domain response of measured signal is:

$$R(f) = SYS(f) \cdot X(f) \tag{3}$$

wherein, $SYS(f)$ is frequency response characteristic of test system, and $R(f)$ is frequency response of measured signal by system.

By the Inverse Fourier Transform of $R(f)$, time domain signal $x_{res}(t)$ output by test system can be obtained as:

$$R(f) \xrightarrow{IFFT} x_{res}(t) \tag{4}$$

The dynamic error of this input signal by test system can be estimated as

$$err(t) = x_{res}(t) - x(t) \tag{5}$$

A. DYNAMIC MODEL OF SENSOR AND CHARGE AMPLIFIER

The charge sensor selected in this paper is 21102 impulse measurable sensor produced by B&W. According to its data manual, main parameters are shown in Table 1.

In order to more accurately measure the output of sensor, it is necessary to establish dynamic model of sensor. Modeling method is adopted in this paper. The dynamic of acceleration sensor is generally second-order model, which is applied for calculation in this paper. In terms of data manual, its undamped oscillation frequency is $\omega_n = 2\pi f_n = 130000\pi$, wherein $f_n = 65kHz$. Damping coefficient is not available in data manual. For common piezoelectric sensor, in general, $\zeta < 0.01$, 0.005 is taken in this paper, and the transfer function of sensor is:

$$A_{sen}(S) = \frac{\omega_n^2}{S^2 + 2\zeta\omega_n S + \omega_n^2} \tag{6}$$

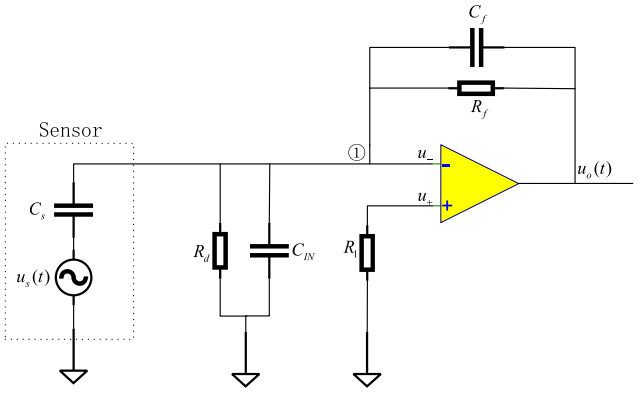

FIGURE 1. The schematic diagram of charge amplifier.

From data manual of sensor, it can be seen that full scale output charge is $Q = (\pm 50000g) \times (-0.5pC/g) = \pm 25000pC$.

The frequency response range is $1 \sim 12000Hz$. The schematic diagram of charge amplifier is shown in Fig. 1, wherein, C_s is interelectrode capacitance, R_d is the parallel value of amplifier input impedance, insulation resistance of transmission conductor and insulation resistance of circuit board, and C_{IN} is the sum of distributed capacitance of circuit board conductor, capacitance of cable and input capacitance of operational amplifier. C_f is the feedback capacitance of charge amplifier, which directly decides the gain of medium frequency band. R_f is not necessary, only for guaranteeing the normal work of amplifier circuit, and avoiding the capacitance voltage saturation caused by cumulative charge of continuous bias current of negative input terminal on capacitance. u_+ and u_- is the voltage of positive and negative input terminal of operational amplifier, respectively.

The circuit model in Fig. 1 can be analyzed according to circuit theory, and transmission characteristic of charge amplifier can be obtained. The plural frequency domain analysis is conducted on circuit. Write a node voltage equation for a ① node column

$$(sC_s+\frac{1}{R_d}+sC_{IN}+\frac{1}{R_f}+sC_f)u_- -(\frac{1}{R_f}+sC_f)u_o = u_s sC_s \tag{7}$$

According to the nature of operational amplifier, it can be seen that

$$A_{od}(u_+ - u_-) = u_o \tag{8}$$

wherein, A_{od} is the open-loop gain of operational amplifier. Due to the input impedance of operational amplifier is large, u_+ can be taken as $0V$. Simultaneous equations (7) and (8) can obtain

$$u_o = \frac{-A_{od}sC_s u_s}{s[(A_{od}+1)C_f + C_s + C_{IN}] + \frac{1}{R_d} + (A_{od}+1)\frac{1}{R_f}} \tag{9}$$

The output charge of sensor is Q, and the relationship between Q and u_s is

$$u_s = \frac{Q}{C_s} \tag{10}$$

From $\omega = 2\pi f$, substitute (10) into (9), and expression form of frequency domain can be

$$u_o = \frac{-j2\pi A_{od} f Q}{j2\pi f[(A_{od}+1)C_f + C_s + C_{IN}] + \frac{1}{R_d} + (A_{od}+1)\frac{1}{R_f}} \tag{11}$$

The amplification A_{charge} of u_o compared to Q is

$$A_{charge} = \frac{u_o}{Q} = \frac{-1}{\frac{1}{A_{od}}(((A_{od}+1)C_f + C_s + C_{IN}) + \frac{1}{j2\pi f}(\frac{1}{R_d} + (A_{od}+1)\frac{1}{R_f}))} \tag{12}$$

When open-loop gain of low frequency and operational amplifier $A_{od} \to \infty$,

$$A_{charge} = \frac{-1}{C_f + \frac{1}{j2\pi f R_f}} = -\frac{1}{C_f} \times \frac{1}{1 - j\frac{\omega_0}{\omega}} = -\frac{1}{C_f} \times \frac{1}{1 - j\frac{f_0}{f}} \tag{13}$$

wherein $\omega_0 = \frac{1}{R_f C_f}, f_0 = \frac{1}{2\pi R_f C_f}$ is its cut-off frequency.

The input impedance of operational amplifier in charge amplifier must be adequately large. The operational amplifier selected in this paper is OPA129 from TI Company. Its open-loop gain is above, $94dB$ with difference-mode input resistance of more than $10^{13}\Omega$. The feedback capacitance C_f decides the gain of medium frequency band. The less the capacitance, the larger the gain. The gain mainly relies on the dynamic range of sensor. The measurement range of 21102 sensor is $\pm 50000g$, and sensitivity is $-0.5pC/g$, so the largest output charge is $\pm 25000pC$. The value of the feedback capacitor in this project is selected as $1nF$. The feedback resistance R_f directly decides the low limiting cut-off frequency of charge amplifier. In order to guarantee a small enough low limiting cut-off frequency, R_f shall be larger. However, it also causes larger output offset voltage. There is input bias current in operational amplifier, so it will form static output offset voltage. Taking input bias current of $10pA$ as an example, if selecting $1G\Omega$ as feedback resistance, output offset voltage can reach $0.01V$, which requires consideration. Besides, larger feedback resistance can also cause larger output noise. After overall consideration, R_f selected by the author in this design is $1G\Omega$. The amplitude-frequency and phase-frequency characteristic curves of A_{charge} in high frequency can be drawn according to Equation (12), shown in Fig. 2.

In low frequency band, the open-loop gain of common operational amplifier is above 10^5. According to

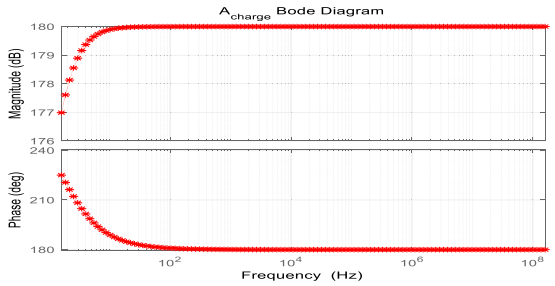

FIGURE 2. Amplitude-frequency and phase-frequency characteristic curves of A_{charge} in high frequency.

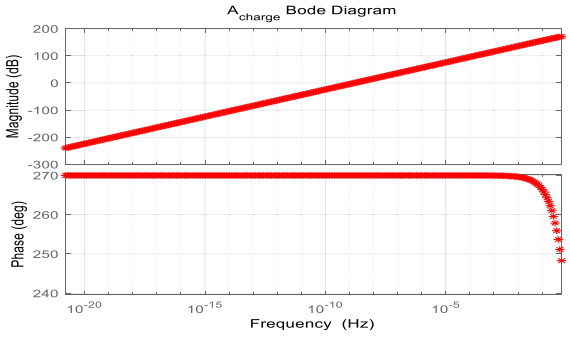

FIGURE 3. Amplitude-frequency and phase-frequency characteristic curves of A_{charge} in low frequency.

Equation (13), the cut-off frequency in low frequency can be obtained as

$$f_{LC} = \frac{1}{2\pi C_f R_f} \tag{14}$$

According to Equation (13), the amplitude-frequency and phase-frequency characteristic curves of A_{charge} can be drawn and shown in Fig. 3. When frequency draws close to $0Hz$, $A_{charge} \to \infty$, and the amplitude significantly declines, so it can be seen that charge amplifier cannot be applied to amplify direct current signal. When there is interference from large direct current component in input terminal, it will not have impact on output terminal. Based on $C_f = 1nF, R_f = 1G\Omega$ before, according to Equation (14), its low limiting cut-off frequency can be estimated. If low limiting cut-off frequency is higher, it cannot match that of sensor. Larger feedback capacitance R_f can be selected to decline low limiting cut-off frequency.

$$f_{LC} = \frac{1}{2\pi \times 1 \times 10^{-9} \times 1 \times 10^{9}} = 0.1592Hz \tag{15}$$

B. DYNAMIC MODEL OF FILTER

From data manual of sensor, the installing resonant frequency of sensor is 65KHz, and the response frequency is 0∼12KHz, so filter is applied to filter natural oscillation and some mechanical vibration signal of measured target and realize anti-alias filtering. The common filter consists of Bessel, Butterworth and Chebyshew. Low-pass filter shall be adopted in order to filter signal above 12KHz. The standard transfer function of second-order filter is shown in Equation (16):

$$A(S) = \frac{m_0 + m_1 S + m_2 S^2}{1 + n_1 S + n_2 S^2} \tag{16}$$

wherein, $n_2 \neq 0$. The expression form in frequency domain is

$$\dot{A}(j\omega) = \frac{m_0 + m_1 j\omega + m_2 (j\omega)^2}{1 + n_1 j\omega + n_2 (j\omega)^2} = \frac{(m_0 - m_2\omega^2) + j m_1 \omega}{(1 - n_2\omega^2) + j n_1 \omega} \tag{17}$$

Introduce characteristic frequency $\omega_0 = \frac{1}{\sqrt{n_2}}$, and substitute ω_0 into Equation (17), Equation (18) can be obtained.

$$\dot{A}(j\omega) = \frac{d + bj\frac{\omega}{\omega_0} + c(j\frac{\omega}{\omega_0})^2}{1 + aj\frac{\omega}{\omega_0} + (j\frac{\omega}{\omega_0})^2} \tag{18}$$

wherein, $a = \frac{n_1}{\sqrt{n_2}}; b = \frac{m_1}{\sqrt{n_2}}; c = \frac{m_2}{\sqrt{n_2}}; d = \frac{m_0}{\sqrt{n_2}}$.

Let $\Omega = \frac{\omega}{\omega_0} = \frac{f}{f_0}$, which represents the specific value of input frequency and characteristic frequency of filter, substituted into Equation (18), Equation (19) can be obtained.

$$\dot{A}(j\Omega) = \frac{d + bj\Omega + c(j\Omega)^2}{1 + aj\Omega + (j\Omega)^2} \tag{19}$$

When $b = 0, c = 0$ in Equation (19), it becomes second-order low-pass filter.

$$\dot{A}(j\Omega) = \frac{A_m}{1 + aj\Omega + (j\Omega)^2} \tag{20}$$

The angular frequency form and frequency form of Equation (20) is shown in Equation (21) and (22), respectively.

$$\dot{A}(j\omega) = \frac{A_m}{1 + aj\frac{\omega}{\omega_0} + (j\frac{\omega}{\omega_0})^2} \tag{21}$$

$$\dot{A}(jf) = \frac{A_m}{1 + aj\frac{f}{f_0} + (j\frac{f}{f_0})^2} \tag{22}$$

Equation (20), (21) and (22) are identical, and just the units of independent variable are different. When $\Omega = 0$, $\omega = 0$ or $f = 0$, $\dot{A} = A_m$; whereas, when $\Omega = \infty$, $\omega = \infty$ or $f = \infty$, $\dot{A} = \frac{A_m}{1+aj\infty+(j\infty)^2} = \frac{A_m}{1-\infty^2+aj\infty} \approx 0$; thus, it satisfies the condition for low-pass filter. When signal frequency f is equal to characteristic frequency f_0, that is $f = f_0$, $\dot{A}(jf) = \frac{A_m}{aj}$, showing that there is just imaginary part for gain, the mode of gain is $\left|\dot{A}(jf)\right| = \left|\frac{A_m}{aj}\right| = \frac{A_m}{a}$, and quality factor Q is defined as the specific value of mode of gain in characteristic frequency and medium-frequency gain A_m, that is

$$Q = \frac{\left|\dot{A}(jf)\right|}{A_m} \tag{23}$$

For second-order low-pass filter, its quality factor $Q = \frac{\left|\dot{A}(jf)\right|}{A_m} = \frac{1}{a}$, so the frequency expression form of second-order low-pass filter can be written as

$$\dot{A}(jf) = \frac{A_m}{1 + \frac{1}{Q}j\frac{f}{f_0} + (j\frac{f}{f_0})^2} \tag{24}$$

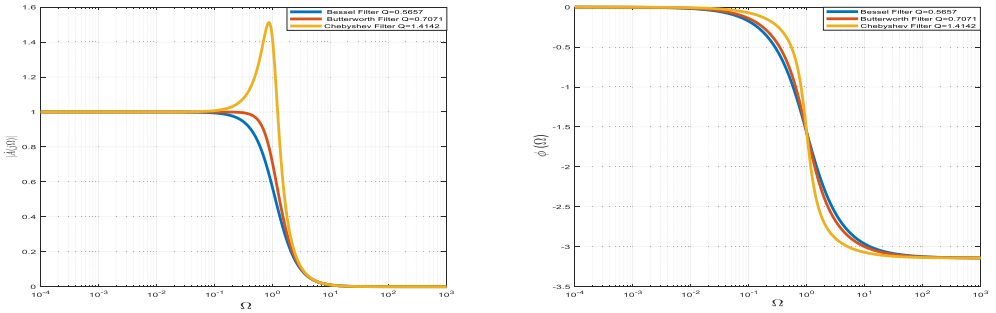

FIGURE 4. Amplitude-frequency and phase-frequency characteristic curves of Bessel, Butterworth and Chebyshev filters.

TABLE 2. Three different types of second-order low-pass filter.

Characteristics	Name
$Q < \frac{1}{\sqrt{2}}$	Bessel Filter
$Q = \frac{1}{\sqrt{2}}$	Butterworth Filter
$Q > \frac{1}{\sqrt{2}}$	Chebyshev Filter

In terms of standard second-order low-pass filter, the nature of different quality factors Q is different. According to different Q, second-order low-pass filter can be divided into Bessel, Butterworth and Chebyshev. Table 2 shows different second-order low-pass filters with different value of Q.

According to Equation (20), there are Bessel, Butterworth and Chebyshev second-order low-pass filters due to different values of Q (take same value for characteristic frequency of three filters). Amplitude-frequency and phase-frequency characteristic curves of three filters are drawn. Form Fig. 4, when characteristics frequency f_0 is identical, Butterworth filter have the flattest passband interval, and the decending rate in transitional band is between that of Butterworth and Chebyshev filters. There is uplift of gain in range of passband of Chebyshev filter, but its descending rate in transitional band is the rapidest one; the descending rate of Bessel filter in transitional band is slowest, but it has biggest linear phase shift interval, which can reduce phase distortion.

Group delay changes with frequency, used to describe that whether the delay of a filter caused by input signal in different frequencies is consistent or not, and its mathematical expression form is

$$t_{gd} = -\frac{d\varphi(\omega)}{d\omega} \tag{25}$$

wherein, $\varphi(\omega)$ is the phase shift of filter, and ω is the angular frequency of input signal of filter. In order to show group delay in normalization form, take the specific value of group delay and corresponding period T_0 of characteristic frequency

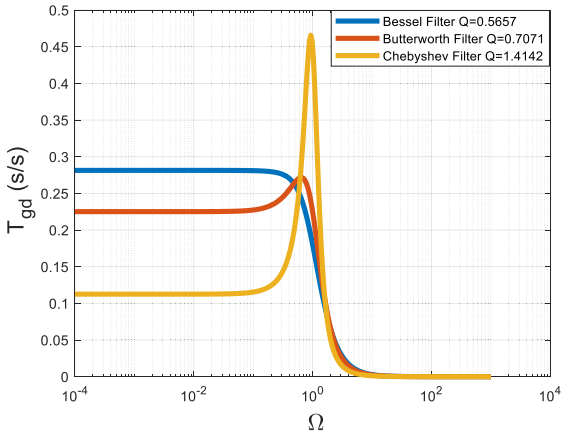

FIGURE 5. The delay time of three second-order low-pass filters.

of filter, shown in

$$T_{gd} = \frac{t_{gd}}{T_0} = t_{gd} \times f_0 = t_{gd} \times \frac{\omega_0}{2\pi} \tag{26}$$

Substitute Equation (25) into Equation (26), and the normalized group delay can be obtained as

$$T_{gd} = -\frac{1}{2\pi} \times \frac{d\varphi}{d\Omega} \tag{27}$$

For second-order low-pass filter in the form in Equation (20), solve the phase and obtain

$$\varphi(\Omega) = -\tan^{-1}\left(\frac{\frac{1}{Q}\Omega}{1-\Omega^2}\right) \tag{28}$$

Substitute Equation (28) into Equation (27), and obtain

$$T_{gd} = \frac{1}{2\pi Q} \times \frac{1+\Omega^2}{1+(\frac{1}{Q^2}-2)\Omega^2+\Omega^4} \tag{29}$$

According to Equation (29), delay curves of Bessel, Butterworth and Chebyshev second-order low-pass filters can be drawn as Fig. 5.

The group delay equal interval of Bessel second-order low-pass filter is longest, which signal in different frequencies. Compared to the other two, Bessel filter can reduce the phase distortion caused by delay to lowest.

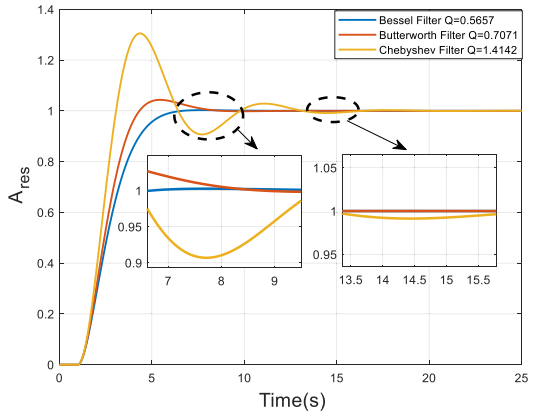

FIGURE 6. The step response of three second-order low-pass filters.

Fig. 6 and Fig. 7 is step response and impulse response of three second-order low-pass filters, respectively. It can be seen that whether step response or impulse response, the ascending and descending rate of Chebyshev filter is rapidest, but there is damping oscillation, requiring longest time to reach stability; the ascending and descending rate of Butterworth filter is between the other two, and there is smaller oscillation, and the required time for stability also between the other two; the ascending and descending rate of Bessel filter is slowest, requiring shortest time for stability, with stable ascent and descent, and there is no oscillation.

The measurement of projectile penetration signal is studied in this paper. The output signal of sensor is generally steep, and the ascending and descending rate are rapid. There is temporary small oscillation for Butterworth filter, larger oscillation for Chebyshev filter, but no oscillation for Bessel filter, which requires shortest time for stability, with smallest peak error. There is longest group delay equal interval for Bessel filter, causing smallest distortion after Bessel filter when penetrating the signal with rapid ascending and descending rate. For common charge sensor, installing resonant frequency is generally far larger than the upper limit of working band. For example, the working band of the sensor selected for the system designed in this paper is 0∼12KHz, and installing resonant frequency is 65KHz. The purpose of filter is to filter resonant noise caused by resonant. After considering above factors, Bessel filter is the optimal choice.

From data manual of selected sensor, it can be known that the working band of sensor is 0∼12khz, so the cut-off frequency is set to be 12KHz. The normalized calculation from Equation (18) to Equation (29) is to be solved according to characteristic frequency. In actual application, cut-off frequency is critical for designing filter. From Equation (24), when $f = f_c$.

$$\left|\dot{A}(jf_c)\right| = \left|\frac{A_m}{1 + \frac{1}{Q}j\frac{f_c}{f_0} + (j\frac{f_c}{f_0})^2}\right| = \frac{\sqrt{2}}{2}A_m \tag{30}$$

wherein, f_c is cut-off frequency, and solve Equation (30) to obtain,

$$\frac{f_c}{f_0} = \frac{\sqrt{4Q^2 - 2 + \sqrt{4 - 16Q^2 + 32Q^4}}}{2Q} \tag{31}$$

When quality factor Q is known, the specific value of cut-off frequency and characteristic frequency is determined. Characteristic frequency is easily to be determined, so it is easy to design filter according to characteristic frequency. When it is determined, corresponding cut-off frequency can be obtained according to the specific value, and vice versa.

In terms of the selection of filter order, it is not right that the higher the order, the better the filter. Fig. 8 shows the step response of second-order, fourth-order and sixth-order Bessel filter. The ascending rate of second-order filter is highest, requiring shortest time for stability. The higher the order, the slower the ascending rate, and the longer the time for stability. Fig. 9 shows the amplitude-frequency curves of second-order, fourth-order and sixth-order Bessel filter. It can

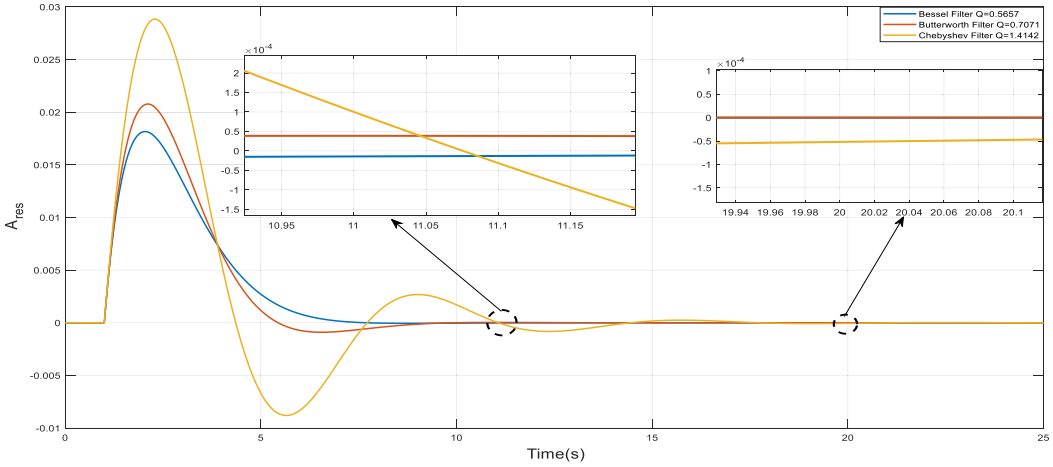

FIGURE 7. The impulse response of three second-order low-pass filters.

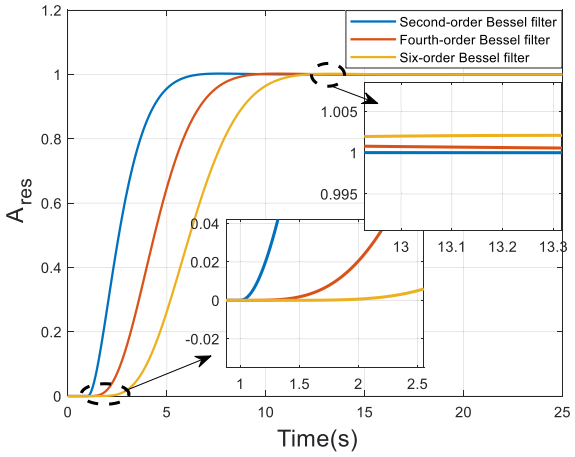

FIGURE 8. The step response of Bessel filter in different orders.

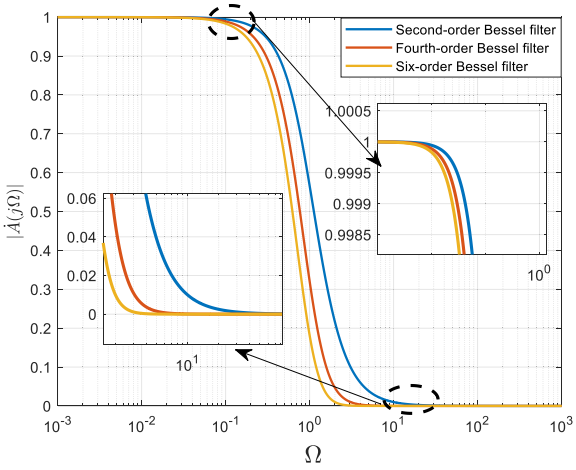

FIGURE 9. The amplitude-frequency curve of Bessel filter in different orders.

be seen that the higher the order, the faster the descending rate of transitional band. The main purpose of designing filter in this paper is to filter the resonant noise caused by installing resonant. The installing resonant frequency of filter in this paper is far larger than the maximum value of working band of sensor, therefore, second-order Bessel low-pass filter can be selected to satisfy the requirement. For lower installing resonant frequency, the order of filter can be added to increase the descending rate of transitional band, so as to better restrain resonant noise.

In this paper, the second-order Bessel low-pass filter is implemented by SK-type low-pass filter, and its circuit diagram is shown in Fig. 10. According to the "virtual short" nature of operational amplifier, the following Equation is established.

$$U_O(S) = U_x(S)\frac{\frac{1}{SC_2}}{R_2 + \frac{1}{SC_2}} \tag{32}$$

The KCL formulation in u_x node is shown in Equation.

$$\frac{U_i(S) - U_x(S)}{R_1} = \frac{U_x(S) - U_O(S)}{\frac{1}{SC_1}} + \frac{U_x(S)}{R_2 + \frac{1}{SC_2}} \tag{33}$$

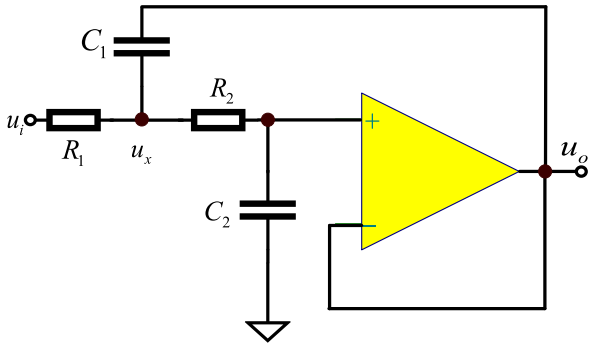

FIGURE 10. The circuit diagram of SK low-pass filter.

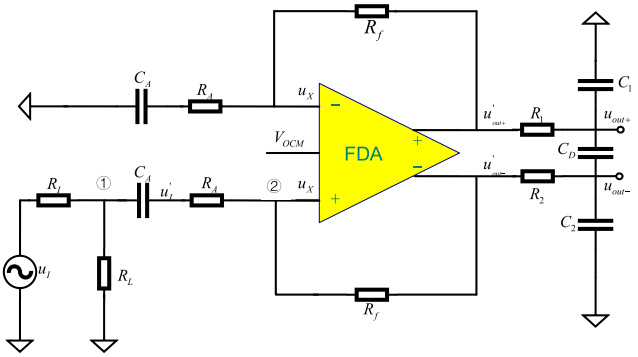

FIGURE 11. The circuit diagram of fully differential operational amplifier realizing signal transformation.

According to Equation (32) and (33), the transfer function of SK filter can be obtained as Equation (34).

$$A_{SK}(S) = \frac{1}{1 + SC_2(R_1 + R_2) + S^2C_1C_2R_1R_2} \tag{34}$$

According to Equation (34), characteristic frequency f_{0_SK} and quality factor Q_{SK} of SK filter can be obtained as Equation (35).

$$f_{0\_SK} = \frac{1}{2\pi\sqrt{C_1C_2R_1R_2}}, \quad Q_{SK} = \frac{\sqrt{C_1C_2R_1R_2}}{C_2(R_1 + R_2)} \tag{35}$$

Its cut-off frequency can be obtained according to characteristic frequency f_{0_SK} and quality factor Q_{SK} . To appropriately select R_1, R_2, C_1 and C_2, and the required filter can be designed.

C. DYNAMIC MODEL OF FULLY DIFFERENTIAL OPERATIONAL AMPLIFIER

In order to increase the noise immunity of circuit and enhance the measurement accuracy of system, AD7768 produced by ADI is adopted in this system. This ADC is configured as differential input, hence, it is necessary to transform signal output by charge amplifier to differential signal, so as to fully give play to the function of ADC. Fully differential operational amplifier is adopted in this paper to realize the transformation of single-ended signal to differential signal. Fig. 11 shows the circuit diagram of fully differential operational amplifier realizing signal transformation.

In Fig. 11, R_A, R_f, R_L and C_A can realize the fully differential amplification and electrical level translation. The first-order passive low-pass filter composed of R_1 and C_1, R_2 and C_2, to filter u_{out+} and u_{out-}, respectively, so as to realize anti-alias filtering and constitute high-order filter with previous order filter, increase the descending rate of transitional band and better filter installing resonant noise of sensor. The first-order passive low-pass difference-mode filter consisting of $R_1 + R_2$ and C_D can filter the difference value of u_{out+} and u_{out-}.

R_I is the output resistance of output signal of previous order circuit, C_A is mainly to stop direct current and connect alternating current, that is to complete alternating current coupling with previous order circuit. When signal frequency is higher, C_A is considered as short circuit. In terms of circuit in Fig. 11, if gain G is given, appropriately select feedback resistor R_f. When satisfying impedance matching, the voltage of left side of R_A is $0.5u_I$, and there is Equation.

$$\frac{u_{out+} - u_{out-}}{0.5u_I} = \frac{R_f}{R_A} = 2G \tag{36}$$

According to the nature of differential operational amplifier, Equation (37) can be obtained.

$$\frac{u_{out+} + u_{out-}}{2} = V_{OCM} \tag{37}$$

According to the nature of ''virtual short'' of fully differential operational amplifier, it can be known that the voltage of positive and negative phase input terminal is approximately equal, $u_P = u_N = u_X$.the input resistance in right side of C_A is solved first, supposed to be, the voltage on the right side of C_A is u'_I, and the formula of positive and negative phase input terminal can be obtained as Equation (38) and (39).

$$\frac{u'_I - u_X}{R_A} = \frac{u_X - u_{out-}}{R_f} \tag{38}$$

$$\frac{0 - u_X}{R_A} = \frac{u_X - u_{out+}}{R_f} \tag{39}$$

Simultaneous equations (37), (38) and (39) can obtain Equation.

$$u_X = \frac{R_f u'_I + 2R_A V_{OCM}}{2R_A + 2R_f} \tag{40}$$

The current flowing past R_A is

$$i_A = \frac{u'_I - u_X}{R_A} = \frac{u'_I}{\frac{R_A(R_A+R_f)}{R_A+0.5R_f}} + \frac{V_{OCM}}{R_A + R_f} \tag{41}$$

When input signal u'_I changes by, $\Delta u'_I$ the current flowing past R_A also changes correspondingly:

$$\Delta i_A = \frac{\Delta u'_I}{\frac{R_A(R_A+R_f)}{R_A+0.5R_f}} \tag{42}$$

The equivalent input resistance R'_i in right side of C_A is:

$$R'_i = \frac{\Delta u'_I}{\Delta i_A} = \frac{R_A(R_A + R_f)}{R_A + 0.5R_f} \tag{43}$$

The transfer function of output terminal and input terminal is:

When frequency is higher, C_A is considered as short circuit. When the input resistance in right side of signal input terminal R_I is r_I, and the impedance matching realized by circuit is required to be equal to output impedance R_I of signal, that is:

$$r_I = \frac{R_L R'_i}{R_L + R'_i} = R_I \tag{44}$$

Node voltage formula can be obtained in point ① and ② as

$$\begin{cases} (\frac{1}{R_I} + \frac{1}{R_L} + \frac{1}{\frac{1}{SC_A} + R_A})u_{n1} - \frac{1}{\frac{1}{SC_A} + R_A}u_{n2} = \frac{u_I}{R_I} \\ -\frac{1}{\frac{1}{SC_A} + R_A}u_{n1} + (\frac{1}{\frac{1}{SC_A} + R_A} + \frac{1}{R_f})u_{n2} \\ \qquad -\frac{1}{R_f}u'_{out-} = 0 \end{cases} \tag{45}$$

From ''virtual short'' nature, it can be seen that the voltage of positive and negative phase input terminal is approximately equal, $u_P = u_N = u_X$. according to the nature of output terminal of fully differential operational amplifier, Equation(46) can be obtained.

$$\begin{aligned} u_X &= u'_{out+}\frac{\frac{1}{SC_A} + R_A}{\frac{1}{SC_A} + R_A + R_f} \\ &= -u'_{out-}\frac{\frac{1}{SC_A} + R_A}{\frac{1}{SC_A} + R_A + R_f} \end{aligned} \tag{46}$$

$$\begin{aligned} A_1(S) = &\frac{R_f}{(R_E + \frac{1}{SC_A} + R_A)(1 + \frac{R_I}{R_L})} \\ &\cdot\frac{1}{1 - \frac{R_f R_E}{2(R_E + \frac{1}{SC_A} + R_A)(R_f + \frac{1}{SC_A} + R_A)}} \end{aligned} \tag{47}$$

wherein, $R_E = R_I // R_L = \frac{R_I R_L}{R_I + R_L}$. From Equation (47), it can be known that when frequency is low, the second item is approximately equal to 1, so the low limiting cut-off frequency mainly depends on the first item, which is f_L. The second item is slightly larger than 1 in low frequency, so the actual low limiting cut-off frequency is slightly larger than f_L, which is:

$$f_L = \frac{1}{2\pi(R_E + R_A)C_A} \tag{48}$$

The transfer function of first-order passive low-pass filter composed of R_1 and C_1, R_2 and C_2 is:

$$A_2(S) = \frac{\frac{1}{SC_1}}{\frac{1}{SC_1} + R_1} = \frac{\frac{1}{SC_2}}{\frac{1}{SC_2} + R_2} \tag{49}$$

wherein $C_1 = C_2, R_1 = R_2$, which that is guarantees the same filter in two output terminals. The overall transfer function of circuit in Fig. 11 is

$$A_{FDA}(S) = A_1(S)A_2(S) \tag{50}$$

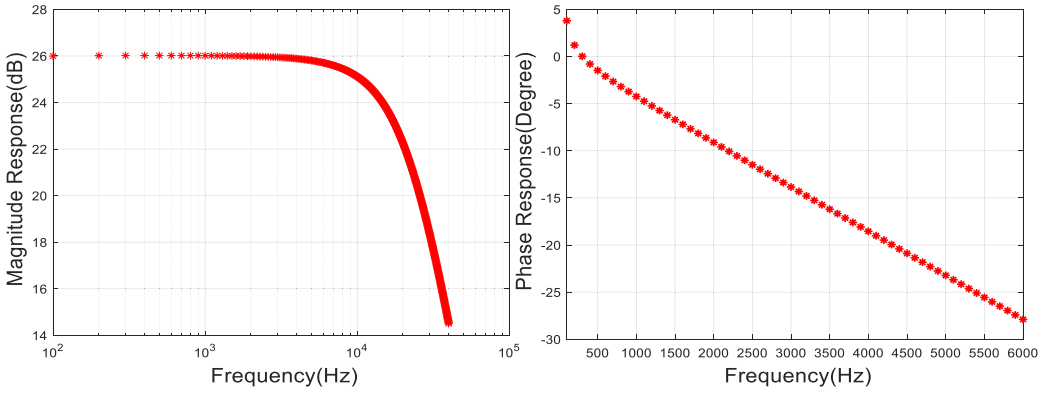

FIGURE 12. Amplitude-frequency and phase-frequency characteristic curves of filter module.

The output of filter is considered as the input of fully differential operational amplifier, so the transfer function after combining the two stages is:

$$A_{filter}(S) = A_{FDA}(S)A_{SK}(S) \tag{51}$$

Relative error is:

$$E(f) = \frac{\left|A_{filter}(f)\right| - A_{FDA}A_{SK}}{A_{FDA}A_{SK}} \tag{52}$$

Fig. 12 shows the amplitude-frequency and phase-frequency characteristic curves of two-stage module. It can be seen that within the effective bandwidth of sensor (12KHz), the passband of amplitude-frequency characteristic curve is sufficiently flat, and phase-frequency characteristic curve is close to be a straight line, with consistent frequency delay. It can be known that there will not distortion when signal passes filter module; Fig. 13 shows frequency characteristic of relative error of filter module, and the maximum error is about 3.5%.

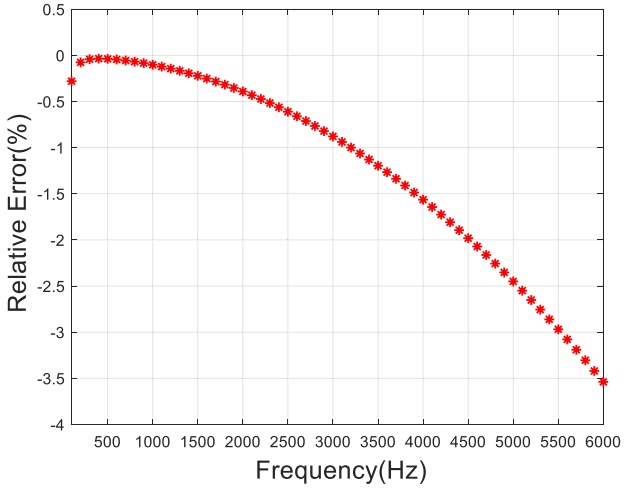

FIGURE 13. Frequency characteristic of relative error of filter module.

III. THE IMPROVED DE-NOISING ALGORITHM BASED ON EEMD

There is a great number of contained installing structure impulse response in projectile penetration overload signal, the impulse response of installing structure shall be filtered to accurately acquire real penetration overload signal. In this paper, an improved de-noising algorithm based on EEMD is proposed, and different low-pass filters are formed on the basis of IMF. The improved de-nosing algorithm of penetration overload signal is established, and its judgment standard shall be formed according to the indicators of dynamic uncertainty and approximation. In terms of the system with poor low-frequency characteristics such as charge amplifier, piecewise calculation is adopted in this paper to realize the comprehensive evaluation of dynamic uncertainty of the test system.

A. DYNAMIC UNCERTAINTY ESTIMATION OF DYNAMIC TEST SYSTEM

The dynamic measurement error of dynamic test system is generally shown by dynamic uncertainty. In order to obtain the measurement accuracy of dynamic test system, it is necessary to estimate the dynamic uncertainty of designed system correctly.

The amplitude-frequency response characteristic of test system is:

$$A_{SYS}(f) = A_{sen}(f) \cdot A_{ch\arg e}(f) \cdot A_{filter}(f) \tag{53}$$

The phase-frequency response characteristic is:

$$\varphi_{sys}(f) = \varphi_{sen}(f) + \varphi_{ch\arg e}(f) + \varphi_{filter}(f) \tag{54}$$

The output of signal $x(t)$ from actual system is $y_r(t)$, the output from ideal system without distortion is $y_i(t)$, and the dynamic error of system is:

$$\varepsilon(t) = y_r(t) - y_i(t) \tag{55}$$

With the error of finite energy and power, the total energy and average power of dynamic error is:

$$W_\varepsilon = \int_{-\infty}^{\infty} \varepsilon^2(t)dt \tag{56}$$

$$P_\varepsilon = \lim_{T\to\infty} \frac{1}{2T} \int_{-\infty}^{\infty} \varepsilon^2(t)dt \tag{57}$$

$\sqrt{P_\varepsilon}$ is called dynamic root-mean-square error or effective value of dynamic error. For time limit signal $x(n)$ with time of duration T_0, average power of error is:

$$P_{\varepsilon d} = \frac{W_\varepsilon}{T_0} = \frac{1}{T_0}\int_{-\infty}^{\infty} \varepsilon^2(t)dt \tag{58}$$

According to Pasval theorem,

$$P_\varepsilon = \overline{\varepsilon^2} = \int_{-\infty}^{\infty} G_\varepsilon(\omega)df \tag{59}$$

The frequency response function of ideal system is $H_i(j\omega)$, actual system is $H_i(j\omega) + \Delta H(j\omega)$, power spectral density of signal is $G_x(j\omega) = |X(j\omega)|^2$, and dynamic error is caused by $\Delta H(j\omega)$ deviating from ideal system:

$$G_\varepsilon(\omega) = G_x(j\omega) \cdot |\Delta H(j\omega)|^2 \tag{60}$$

Error power is:

$$P_{\varepsilon d} = \frac{W_\varepsilon}{T_0} = \frac{1}{T_0}\int_{-\infty}^{\infty} |X(j\omega)|^2 |\Delta H(j\omega)|^2 df \tag{61}$$

$\Delta H(j\omega)$ can be solved by, frequency characteristic of actual system is:

$$H_r(j\omega) = K_r(\omega)e^{j\varphi_r(\omega)} \tag{62}$$

$K_r(\omega)$ is amplitude-frequency characteristic of actual system, $K_r(\omega) = |H_r(j\omega)|$, $\varphi_r(\omega)$ is phase-frequency characteristic of actual system. The frequency characteristic of ideal system is:

$$H_i(j\omega) = K_i e^{j\varphi_i(\omega)} \tag{63}$$

The amplitude-frequency characteristic of ideal system in working band is steady-state value, and $\varphi_1(\omega)$ is phase-frequency characteristic of ideal system. The relationship between amplitude-frequency and phase-frequency characteristic of ideal system and actual system is respectively:

$$\Delta\varphi(\omega) = \varphi_r(\omega) - \varphi_i(\omega) \tag{64}$$

$$\Delta K(\omega) = K_i - K_r(\omega) \tag{65}$$

In Nyquist diagram, $H_r(j\omega)$, $H_i(j\omega)$ and $\Delta H(j\omega)$ constitute a triangle. The included angle of $H_r(j\omega)$ and $H_i(j\omega)$ is $\Delta\varphi(\omega)$. According to Cosine Law:

$$|\Delta H(j\omega)|^2 = K_r^2 + K_i^2 - 2K_iK_r\cos(\Delta\varphi(\omega)) \tag{66}$$

Substitute Equation (65) into Equation (66), and there is:

$$|\Delta H(j\omega)|^2 = 2[(K_r(\omega))^2 + K_r(\omega)\cdot\Delta K(\omega)] \cdot(1 - \cos(\Delta\varphi(\omega))) + (\Delta K(\omega))^2 \tag{67}$$

In terms of charge amplifier, there is larger error in low frequency band, because the low limiting cut-off frequency of charge amplifier in low frequency band is $f_{LC} = \frac{1}{2\pi C_f R_f}$. Piecewise calculation is adopted for charge amplifier with poor low-frequency characteristic:

$$P_\varepsilon = \sum_{f=0}^{f_{LC}} |\Delta X_{LC}(j\omega)|^2\Delta f + \sum_{f=f_{LC}}^{f_m} |\Delta X_{HC}(j\omega)|^2\Delta f \tag{68}$$

wherein, f_{LC} is low-frequency cut-off frequency, Δf is smallest frequency step length, $\Delta X_{LC}(j\omega)$ is the vector difference of frequency characteristic in low frequency band, and $\Delta X_{HC}(j\omega)$ is the vector difference of frequency characteristic in high frequency band.

B. THE DESIGN OF IMPROVED DE-NOISING ALGORITHM

After the EEMD decomposition of penetration overload signal with noise $y_r(t)$ acquired by system measurement, the reconstructing signal is shown in Equation (69).

$$\mathrm{y}_r(t) = \sum_{i=1}^{n} IMF_i(t) + r_n(t) \tag{69}$$

wherein, $IMF_i(t)$ is Intrinsic Mode Function; $r_n(t)$ is remainder term; n is the number of Intrinsic Mode Function. The low-pass filter can be designed as Equation (70).

$$LP_k = \sum_{i=k}^{n} IMF_i(t) + r_n(t) \tag{70}$$

The high-pass filter can be designed as Equation (71).

$$HP_P = \sum_{i=1}^{p} IMF_i(t) \tag{71}$$

Similarly, the band-pass filter can be designed as Equation (72).

$$BP_b^q = \sum_{i=b}^{q} IMF_i(t) \tag{72}$$

wherein, p, q is the upper cut-off parameter, and k, b is the lower cut-off parameter. The value shall be optimized and determined according to signal characteristics and filter requirements.

The penetration overload signal with noise acquired by system measurement can be written as Equation (73).

$$y_r = (y_{r1}, y_{r1}, \cdots, y_m) \tag{73}$$

The de-noising deviation mean square error of algorithm is defined as Equation (74).

$$MES_f = \sqrt{\frac{\sum_{j=1}^{m}(\hat{y}_{rj} - y_{rj})^2}{m}} \tag{74}$$

wherein, y_{rj} is the penetration overload signal with noise acquired at j time, $j = 1, 2, \cdots, m$; m is the total number of sampled signal; $\hat{y}_{rj}$ is the de-noising result of y_{rj} by algorithm, $j = 1, 2, \cdots, m$.

Considering when MSE_f equals to zero, the reciprocal of $(MSE_f + 1)$ is called approximation of the algorithm, noted as MSE_f^{-1}. It can be known that $0 < MSE_f^{-1} \leq 1$, the smaller the de-noising deviation mean square error MSE_f, the closer to 1 the MSE_f^{-1}, and the closer to original signal the de-noising result.

In terms of the de-noising of penetration overload signal, it is necessary to consider the de-noising effect, also whether

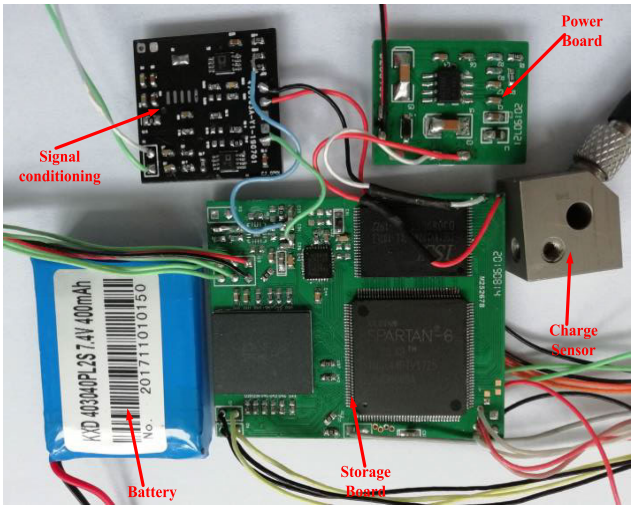

FIGURE 14. Circuit board.

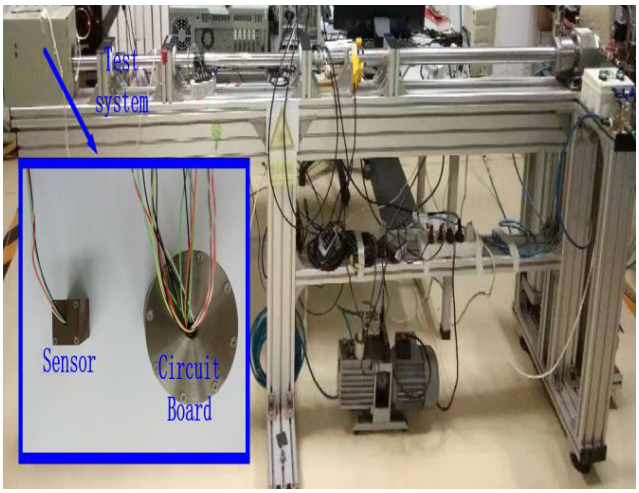

FIGURE 15. Standard test based on Hopkinson bar.

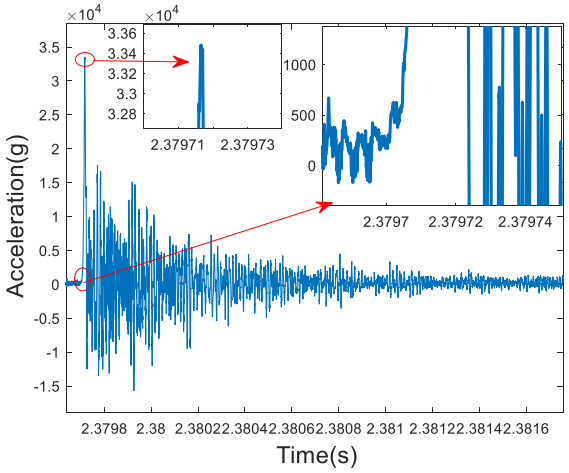

FIGURE 16. The output signal of sensor measured by designed system.

the wave form after de-noising closely related to real signal. The smaller the dynamic uncertainty estimation $\sqrt{p_\varepsilon}$, the closer to ideal penetration overload signal the de-noising result.

The de-noising result is hoped to be fully similar to ideal penetration overload signal (that is, if the smaller dynamic uncertainty $\sqrt{p_\varepsilon}$ the better, the larger $\frac{1}{\sqrt{p_\varepsilon}}$ the better), and better de-noising effect is demanded (that is the larger approximation MSE_f^{-1}, the better). However, it is difficult to realize the two indicators at the same time, thus, the judgment standard of improved de-noising algorithm is established as followed:

Constraint condition:

$$\begin{cases} \max\left\{\dfrac{1}{\sqrt{p_\varepsilon}}\right\} \\ \max\left\{\left|\rho_f\right|\right\} \end{cases} \tag{75}$$

The objective function of de-noising algorithm f is shown as Equation (76).

$$\max\{f\} = \max\left\{\frac{\alpha}{\sqrt{p_\varepsilon}} + (1-\alpha)\left|\rho_f\right|\right\} \tag{76}$$

wherein, α, $1-\alpha$ is the impact factor of dynamic uncertainty and approximation, respectively. The selected weight is determined according to specific requirement of signal processing.

IV. EXPERIMENTAL RESULTS

According to the method proposed in this paper, parameters of components and parts of circuit can be determined, further the circuit board can be produced as Fig. 14, mainly consisting of sensor, signal processing circuit, acquisition and storage circuit, battery and power control circuit. Specifically, sensor is separately installed in a cubic structural body, and signal processing circuit, acquisition and storage circuit, battery and power control circuit are installed in a cylindrical structural body as Fig. 15. In this way, measurement circuit can be better protected to effectively read data after testing.

Fig. 15 shows the standard test based on Hopkinson bar. The Hopkinson bar applied in this test is made of titanium alloy with the diameter of $\Phi 16mm$ and length of $1600mm$. Waveform adjusting shim and acceleration soleplate are closely pulled in two sides of Hopkinson bar by industrial silicone grease and vacuum fixture. The raster is pasted on the periphery of accelerometer soleplate as the cooperative target of diffraction. The laser interferometer is pasted on diffraction grating of soleplate as cooperative target to measure the prompting acceleration. Fig. 16 shows the output signal of sensor measured by designed system. Fig. 17 shows the test data curve of laser interferometer. It can be seen hat the prompting accelerating peak measured by designed system is 33320g, pulse width is 18.9us, the acceleration peak measured by laser interferometer is 33800g, and the pulse width is 19.2us. If the test data of laser interferometer is considered as standard value, the pulse acceleration peak error measured by designed test circuit is 1.4%, and pulse width error is 1.5%.

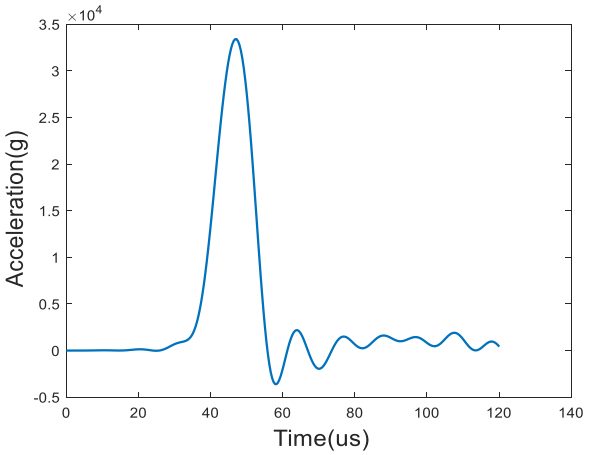

FIGURE 17. The test data curve of laser interferometer.

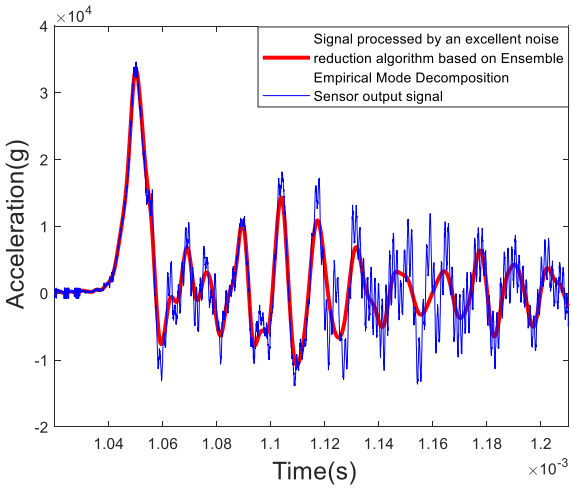

FIGURE 18. Sensor output signal and signal processed by an excellent noise reduction algorithm based on EEMD.

In Figure 18, the red curve is the result processed by improved de-noising algorithm based on EEMD proposed in this paper, and the blue curve is the original information output by sensor. From Figure 19, it can be known that a great number of response of installing is contained in the signal output by sensor. The impact of installing structure can be better removed by de-noising.

V. CONCLUSION

This paper studies the dynamic design principle of projectile penetration overload test system based on charge sensor, according to characteristics of steep front and a great number of contained installing structure impulse response, designs the measuring circuit based on charge sensor, conducts detailed theoretical deduction on dynamic model of sensor, charge-amplifier, filter and single conversion differential circuit, and provides theoretical basis for design. The results show that the pulse acceleration peak error measured by designed measuring circuit is 1.4%, and pulse width error is 1.5%. In order to more objectively evaluate the dynamic characteristics of this kind of test system, the dynamic uncertainty estimation of charge signal measured by this test system is considered as the standard for evaluating its dynamic characteristics. Instead of simply considering the unflatness of amplitude-frequency characteristic and its width in frequency domain as the standard to evaluate the dynamic characteristic of this system, the comprehensive evaluation on uncertainty of this test system is realized. In this paper, an improved de-noising algorithm based on EEMD is proposed, different low-pass filters are formed on the basis of IMF, and the measured data of sensor is analyzed and processed via the improved de-noising algorithm proposed. It can be seen from experiment results that this method can realize better de-noising effect and effectively remove the impact of installing structure on sensor. Making the most of the sensor's performance.

The measurement of penetration overload signal based on charge sensor is deeply studied in this paper. The experiment results is of theoretical and applied significance to evaluating the reasonableness and effectiveness of measurement method of penetration overload signal and seeking for improved processing method of penetration overload signal with noise.

REFERENCES

[1] D. J. Frew, M. J. Forrestal, and J. D. Cargile, "The effect of concrete target diameter on projectile deceleration and penetration depth," *Int. J. Impact Eng.*, vol. 32, no. 10, pp. 1584–1594, 2006.

[2] M. J. Forrestal, B. S. Altman, J. D. Cargile, and S J. Hanchak, "An empirical equation for penetration depth of ogive-nose projectiles into concrete targets," *Int. J. Impact Eng.*, vol. 15, pp. 395–405, 1994.

[3] M. J. Forrestal, D. J. Frew, S. J. Hanchak, and N. S. Brar, "Penetration of grout and concrete targets with ogive-nose steel projectiles," *Int. J. Impact Eng.*, vol. 18, pp. 465–476, 1996.

[4] D. J. Frew, S. J. Hanchak, M. L. Green, and M. J. Forrestal, "Penetration of concrete targets with ogive-nose steel rods," *Int. J. Impact Eng.*, vol. 21, pp. 489–497, 1998.

[5] M. J. Forrestal, D. J. Frew, and J. P. Hickerson, "Penetration of concrete targets with deceleration-time measurements," *Int. J. Impact Eng.*, vol. 28, no. 5, pp. 479–497, 2003.

[6] T. L. Warren, M. J. Forrestal, and P. W. Randles, "Evaluation of large amplitude deceleration data from projectile penetration into concrete targets," *Exp. Mech.*, vol. 54, no. 2, pp. 241–253, 2014.

[7] H. Wu, Q. Fang, Y. Peng, Z. M. Gong, and X. Z. Kong, "Hard projectile perforation on the monolithic and segmented RC panels with a rear steel liner," *Int. J. Impact Eng.*, vol. 76, pp. 232–250, 2015.

[8] J. Z. Li, Z. J. Lv, H. S. Zhang, and F. L. Huang, "Perforation experiments of concrete targets with residual velocity measurements," *Int. J. Impact Eng.*, vol. 57, pp. 1–6, 2013.

[9] Z. C. Lu and H. M. Wen, "On the penetration of high strength steel rods into semi-infinite aluminium alloy targets," *Int. J. Impact Eng.*, vol. 111, pp. 1–10, 2018.

[10] J. Liu, C. Q. Wu, Y. Su, J. Li, R. Z. Shao, G. Chen, and Z. X. Liu, "Experimental and numerical studies of ultra-high performance concrete targets against high-velocity projectile impacts," *Eng. Struct.*, vol. 173, pp. 166–179, 2018.

[11] X. Chen, F. Lu, and D. Zhang, "Penetration trajectory of concrete targets by ogived steel projectiles–Experiments and simulations," *Int. J. Impact Eng.*, vol. 120, pp. 202–213, Oct. 2018.

[12] J. Liu, C. Q. Wu, J. Li, Y. Su, and X. W. Chen, "Numerical investigation of reactive powder concrete reinforced with steel wire mesh against high-velocity projectile penetration," *Construct. Building Mater.*, vol. 166, pp. 855–872, 2018.

[13] T. Addabbo, A. Fort, M. Mugnaini, E. Panzardi, and V. Vignoli, "A smart measurement system with improved low-frequency response to detect moving charged debris," *IEEE Trans. Instrum. Meas.*, vol. 65, no. 8, pp. 1874–1883, Aug. 2016.

[14] T. Kos, T. Rojac, J. Petrovčič, and D. Vrančić, "Control system for automated drift compensation of the stand-alone charge amplifier used for low-frequency measurement," *AIP Adv.*, vol. 9, no. 3, Mar. 2019, Art. no. 035133.
[15] J. Zhang, L. Zhao, R. S. Dong, P. Deng, C. Ma, J. Lu, and Q. An, "A time-to-digital converter-based correction method for charge measurement through area integration," *IEEE Trans. Nucl. Sci.*, vol. 65, no. 12, pp. 2883–2891, Dec. 2018.
[16] J. Havunen and J. Hällström, "Application of charge-sensitive preamplifier for the calibration of partial discharge calibrators below 1 pC," *IEEE Trans. Instrum. Meas.*, vol. 68, no. 6, pp. 2034–2040, Jun. 2019.
[17] P. Assis, A. Blanco, P. Brogueira, M. Ferreira, and R. Luz, "The MARTA (muon array with RPCs for tagging air showers) front-end acquisition system," *IEEE Trans. Nucl. Sci.*, vol. 65, no. 12, pp. 2920–2928, Dec. 2018.
[18] I. Mahbub, S. Shamsir, S. A. Pullano, A. S. Fiorillo, and S. K. Islam, "Design of a charge amplifier for a low-power respiration-monitoring system," *IET Circuits Devices Syst.*, vol. 13, no. 4, pp. 499–503, 2019.
[19] S. K. Kar, P. Chatterjee, B. Mukherjee, K. Swamy, and S. Sen, "A differential output interfacing ASIC for integrated capacitive sensors," *IEEE Trans. Instrum. Meas.*, vol. 67, no. 1, pp. 196–203, Jan. 2018.
[20] R. Marco-Hernandez, M. Bau, M. Ferrari, V. Ferrari, F. Pedersen, and L. Søby, "A low-noise charge amplifier for the ELENA trajectory, orbit, and intensity measurement system," *IEEE Trans. Nucl. Sci.*, vol. 64, no. 9, pp. 2465–2473, Sep. 2017.
[21] H. B. Zhang, S. Hou, and J. P. Ou, "Smart aggregate-based seismic stress monitoring system using a specially designed charge amplifier," *J. Intell. Mater. Syst. Struct.*, vol. 27, no. 3, pp. 418–426, 2016.
[22] A. Seljak, H. S. Cumming, G. Varner, J. Vallerga, R. Raffanti, and V. Virta, "A fast, low power and low noise charge sensitive amplifier ASIC for a UV imaging single photon detector," *J. Instrum.*, vol. 12, p. 11, 2017.
[23] N. E. Huang, Z. Shen, S. R. Long, M. C. Wu, H. H. Shih, Q. Zheng, N.-C. Yen, C. C. Tung, and H. H. Liu, "The empirical mode decomposition and the Hilbert spectrum for nonlinear and non-stationary time series analysis," *Proc. Royal Soc. A.*, vol. 454, pp. 679–699, Mar. 1998.
[24] N. E. Huang, M.-L. Wu, W. Qu, S. R. Long, and S. S. P. Shen, "Applications of Hilbert–Huang transform to non-stationary financial time series analysis," *Appl. Stochastic Models Bus. Ind.*, vol. 19. pp. 245–268, Jul./Sep. 2003, doi: 10.1002/asmb.501.
[25] Z. Wu and N. Huang, "Ensemble empirical mode decomposition: A noise-assisted data analysis method," *Adv. Adapt. Data Anal.*, vol. 1, no. 1, pp. 1–41, 2009, doi: 10.1142/S1793536909000047.

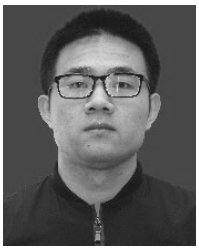

DEBIAO ZHANG was born in Jiaxiang, Shandong, China, in June 1989. He is currently pursuing the Ph.D. degree in instrument science and technology with the School of Instrument and Electronics, North University of China. He is currently study circuits and systems, signal acquisition, and dynamic testing techniques in complex and harsh environments.

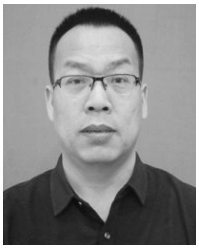

JIE LI was born in Shanxi, China, in 1976. He received the Ph.D. degree in navigation, guidance, and control from the Department of Automatic Control, Beijing Institute of Technology, Beijing, China, in 2005. From April 2006 to June 2009, he was a Postdoctoral Research Associate with the North University of China, Taiyuan, China, and work on navigation, guidance, and control. Since 2007, he has been with the School of Instrument and Electronics, North University of China, first as an Associate Professor, and then, since 2013, has been a Professor. His current research interests include strapdown inertial navigation, integrated navigation, and intelligent information processing.

XIAOKAI WEI was born in Nei Monggol, China, in 1992. He received the B.E. degree in weapon system and launch engineering from the College of Mechatronics Engineering, North University of China, Taiyuan, China, in 2015, where he is currently pursuing the Ph.D. degree in instrument science and technology. His current research interests include inertial navigation, integrated navigation, and adaptive control.

KAIQIANG FENG was born in the Shanxi, China, in 1989. He received the B.E. degree from the School of Instrument and Electronics, North University of China, Taiyuan, China, in 2013, where he is currently pursuing the Ph.D. degree in navigation, guided, and control. His current research interests include inertial navigation, inertial-based integrated navigation systems, and state estimation theory.

YU WANG was born in Shanxi, China, in 1991. He received the B.S. degree from the Inner Mongolia University of Science and Technology, Inner Mongolia, in 2015. He is currently pursuing the Ph.D. degree with the North University of China. His current research interests include magnetically confined plasma and dynamic test.

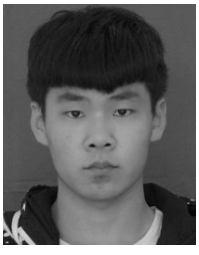

JIHE ZHAO was born in Hebei, China, in 1995. He is currently pursuing the master's degree in instrument science and technology with the North University of China. He is now working on high-speed data recorders.